Testing Rotational Mixing Predictions with New Boron Abundances in Main Sequence B-type Stars

J. T. Mendel[1] and K. A. Venn[2]

Macalester College, 1600 Grand Avenue, Saint Paul, MN, 55105; venn@macalester.edu

C. R. Proffitt[3]

Science Programs, Computer Sciences Corporation, 3700 San Martin Drive, Baltimore, MD 21218; proffitt@stsci.edu

A. M. Brooks

Astronomy Department, University of Washington, Box 351580, Seattle, WA, 98195; abrooks@astro.washington.edu

and

D. L. Lambert

McDonald Observatory, University of Texas, 1 University Station, Austin, TX, 78712-1083; dll@astro.as.utexas.edu

ABSTRACT

New boron abundances for seven main-sequence B-type stars are determined from HST STIS spectroscopy around the B III 2066 Å line. Boron abundances provide a unique and critical test of stellar evolution models that include rotational mixing since boron is destroyed in the surface layers of stars through shallow mixing long before other elements are mixed from the stellar interior

[1]Present address: Centre for Astrophysics and Supercomputing, Swinburne University of Technology, Mail Number 31, P.O. Box 218, Hawthorn, VIC 3122, Australia; tmendel@astro.swin.edu.au

[2]Present address: Department of Physics and Astronomy, University of Victoria, Elliott Building, 3800 Finnerty Road, Victoria, BC, V8P 1A1, Canada; kvenn@uvic.ca

[3]Also at: Space Telescope Science Institute, and Institute for Astrophysics and Computational Science, Catholic University of America

through deep mixing. The stars in this study are all on or near the main-sequence and are members of young Galactic clusters. They show no evidence of mixing with gas from H-burning layers from their CNO abundances. Boron abundances range from 12+log(B/H)≤1.0 to 2.2. The boron abundances are compared to the published values of the stellar nitrogen abundances (all have 12+log(N/H) ≤7.8) and to their host cluster ages (4 to 16 Myr) to investigate the predictions from models of massive star evolution with rotational mixing effects. We find that the variations in boron and nitrogen are generally within the range of the predictions from the stellar evolution models with rotation (where predictions for models with rotation rates from 0 to 450 km s^{-1} and μ-barriers are examined), especially given their age and mass ranges.

Three stars (out of 34 B-type stars with detailed boron abundance determinations), deviate from the model predictions, including HD 36591, HD 205021, and HD 30836. The first two of these stars have much larger boron depletions than are predicted for their spectroscopic masses and very young ages, even adopting the highest rotation rates from the model predictions. HD 36591 also shows no significant nitrogen enhancement, as uniquely predicted by the rotating stellar evolution models. HD 205021, however, has a small nitrogen enrichment which could be explained by stellar rotation or mass transfer since it is in a binary system. The spectroscopic mass for the third star, HD 30836, is marginally lower than expected given the rotating model predictions for its age and boron abundance. This star also has no significant nitrogen enhancement, thus even though it is in a binary system it does not show the nitrogen enrichment expected if it has undergone mass transfer. Therefore, the results from these three stars suggest that rotational mixing could be more efficient than currently modelled at the highest rotation rates.

Subject headings: stars: abundances – stars: evolution – stars: rotation

1. Introduction

Rotation is recognized as an important physical component in understanding the evolution of massive stars and yet is a theoretically challenging problem. Rotation affects the lifetimes, chemical yields, stellar evolution tracks, and the properties of supernova and compact remnants (Heger & Langer 2000; Maeder & Meynet 2000, 2005). The new rotating stellar evolution models also address long standing problems such as the origin of the B[e] and WNL/Ofpe (slash) stars, the distribution of red to blue supergiants on the HR dia-

gram, and the unseen post main-sequence gap predicted in all standard stellar evolution scenarios. With rotation, it is also possible to explain the variations in the surface helium, carbon, nitrogen, and oxygen (He and CNO) abundances in OB stars on and near the main sequence (e.g., Gies & Lambert 1992, Herrero *et al.* 1992, Cunha & Lambert 1994, Dennisenkov 1994, Lyubimkov 1996, Lyubimkov *et al.* 2004). Several of these observations have been used to constrain the various mixing prescriptions used in the new models of massive star evolution with rotation. Additional observations are now necessary to test the model predictions and provide new constraints for the transport of angular momentum and chemical species in rotating massive stars. One avenue of observational testing is to determine the helium and CNO abundances in massive stars in young star clusters in the Galaxy and Magellanic Clouds (Evans *et al.* 2005). This tests the metallicity effects predicted by the models. Another line of research includes the determination of the light element abundances at the surface of massive stars. This tests the earliest stages of rotational mixing (timescales and mixing efficiencies), *before* hot gas from the stellar interior is observable at the surface (Fliegner *et al.* 1996, Venn *et al.* 2002).

The abundances of the light elements, lithium, beryllium, and boron (LiBeB) are known to be sensitive to rotational mixing in both low and high mass stars. LiBeB is destroyed on exposure to protons at temperatures too low for H-burning to have occurred ($\leq 6 \times 10^6$ K), therefore even shallow mixing at the stellar surface induced by rotation can lead to LiBeB depletions. In low mass stars, variations in the surface abundances of all three elements have been traced to rotational mixing (e.g., Boesgaard & Lavery 1986; Pinsonneault 1997). In high mass stars, only boron[1] has been available. Spectroscopy of the B III feature at $\lambda 2066$ using the International Ultraviolet Explorer (IUE) archived spectra or the Hubble Space Telescope (HST) Space Telescope Imaging Spectrograph (STIS) or Goddard High Resolution Spectrograph (GHRS) have made boron abundance determinations possible in B-type stars. Significant variations in the boron abundances in hot, massive stars have been observed (e.g., Proffitt & Quigley 2001, Venn *et al.* 2002).

Boron depletions in B-type stars are predicted to be associated with nitrogen enhancements. This is because mechanisms that can deplete boron at the surface of a star will also mix the surface with CN-cycled gas, i.e., gas from H-burning layers where the CN-cycle has converted carbon into nitrogen. This is true whether boron is destroyed through rotational mixing (where hot CN-cycled gas from the interior is mixed to the surface) or through bi-

---

[1] There are no readily accessible spectral lines of Li in hot stars, and the resonance lines of Be II near 3130Å are predicted to be very weak in B-type stars, and they occur at the atmospheric cutoff, thus these spectra would be difficult to access from ground based telescopes. Currently, there are no published observations of the Be II lines in B-stars.

nary mass transfer (where CN-cycled gas is deposited on the surface of the star; Wellstein 2001). Simple initial abundance variations and mass loss from B-type stars are ruled out (see Venn *et al.* 2002). However, there is one *unique* characteristic of the rotational mixing scenario that makes for an interesting and exciting new observational constraint. Boron depletion occurs *before* nitrogen enhancement. This is because rotational mixing taps the surface boron-free layers first, then subsequent deeper mixing can penetrate layers where H-burning has occured via the CN-cycle, converting carbon into nitrogen. Thus, the initial phases of rotational mixing in stars is revealed by depletions of boron, followed only *later* by nitrogen-enrichment and carbon-depletion, a different signature from binary mass transfer.

Some B-type stars with boron depletions, but no nitrogen enrichments, were found by Venn *et al.* (2002) and intrepreted as concrete and unambiguous evidence for rotational mixing on the main sequence. However, two stars with masses of 12-13 $M_\odot$ showed uncharacteristically large boron depletions. These two stars required models with higher masses (20 $M_\odot$) and the highest rotation rates ($\sim$450 km s^{-1}) to reproduce the boron depletions (from Heger & Langer 2000 models). Since very few stars are expected to rotate at these high speeds, and because of the mass discrepancy, this suggested that rotational mixing may be even more efficient than currently predicted.

Presently, 32 solar neighborhood (see Table 9 in Venn *et al.* 2002) and two stars in the Small Magellanic Cloud (Brooks *et al.* 2002) B-type stars have boron abundance determinations. Of these, only nine have been determined from high quality HST STIS or GHRS spectra of the relatively unblended B III 2066 line. In this paper, we present new boron abundances for seven additional B-type stars from HST STIS spectroscopy. These stars were selected from the group of B-type stars examined with International Ultraviolet Explorer (IUE) that may have low boron abundances (Proffitt & Quigley 2001). They are also all in young galactic clusters (for age estimates), and they show no nitrogen enrichments (12+log(N/H) $\leq$7.8). Therefore, the determination of boron abundances in these stars provides a unique observational test for studying the earliest phases of massive star rotational mixing effects.

2. Target Selection and Observations

Seven B-type stars were observed using HST STIS spectroscopy of the B III feature at λ2066. Previous analyses of the target stars (Gies & Lambert 1992; Cunha & Lambert 1994) show that the targets have normal, unenriched nitrogen abundances in their atmospheres. Analyses of IUE spectra by Proffitt & Quigley (2001) indicate that these targets have very weak or absent B III lines, however the resolution of IUE and signal-to-noise of some of

these spectra make quantitative boron abundances highly uncertain. These 7 stars were also selected from young galactic OB associations in order that effects of rotationally induced mixing could be examined with age. Data considered in the selection of these targets is listed in Table 1.

Spectra for six of the seven targets were gathered using the E230M grating and 0.2x0.05ND slit with a neutral density filter (ND=2) to avoid the MAMA-NUV brightness limits. This grating choice is sufficient to resolve the B III line in all of our targets since the instrumental broadening of this grating is 9 km s^{-1} (given our slit choice), whereas the targets have rotational velocities $\leq$40 km s^{-1}. To attain the best possible signal-to-noise spectra, three different configurations of the E230M grating were used, each with a slightly different central wavelength (λ_c of 1978, 2124, and 2269 Å) so that the B III line landed on different regions of the MAMA detector and subsequent combinations could better reduce pixel noise variations. Echelle observations with the E230M grating included 40 orders; only those orders in the desired wavelength region ($\lambda\lambda$2044-2145) were extracted and combined using standard IRAF[2] packages. Spectra were then normalized using a low order spline3 polynomial; wavelengths listed here are in air and at rest. Exposure times, central wavelengths, and observation dates are listed in Table 2, as well as the signal-to-noise ratio of the final extracted spectra.

The reductions for two stars, HD 36285 and HD 214993, were conducted using procedures different from those described above. HD 36285 (V=6.32) was faint enough to be observed with the higher resolution E230H grating (31x0.05NDA slit), and HD 214993 is a known variable star. The observations and reductions for these two stars are described below.

2.1. HD 36285

Observations of HD 36285 were done using the STIS E230H grating at the λ2013 central wavelength setting. This star was too bright to be observed with any of the clear STIS apertures, but since we desired very high S/N in order to study the ^{10}B/^{11}B isotope ratio (Proffitt et $al.$, in progress), we adopted the unsupported 31X0.05NDA slit, which has an attenuation factor of about 4. The global count rates were 1.2x10^5 to 1.5x10^5 cnts/s per observation, which is modestly under the 2x10^5 cnts/s upper limit allowed for the NUV-MAMA detector. Using a long slit and dithering our subexposures in the cross-dispersion direction along the length of the aperture allowed for higher S/N. Nine different dither

---

[2]IRAF is distributed by the National Optical Astronomy Observatories, which is operated by the Association of Universities for Research in Astronomy, Inc., under cooperative agreement with the National Science Foundation

positions with a spacing between positions of about 0.15" (or about 5 pixels) were used. This averages any fixed pattern noise of flat-fielding errors, and removes any bad pixels or detector defects.

Since the 31X0.05NDA aperture is not a supported aperture, the standard reference files supplied by STScI cannot be used to produce extracted and flux calibrated 1D spectra. While the measured throughput curve of the 31X0.05NDA aperture was used for calculating the scattered light background, we adopted the parameters supplied for the 0.3x0.05ND aperture. In addition, for some of the more extreme dither positions, the reference file which specifies the default locations of spectral orders on the detector had to be edited so that the calstis software could correctly identify each order.

In principle, the use of a long slit with the echelle could increase the amount of interorder scattered light and cause an error in the background subtraction. There are some modest S/N (15 to 20) E230H observations of HD 39060 (β Pic) which were used to check for such effects (Program GO-7512, PI Lagrange; see Roberge et $al.$ 2000). Observation o4g002020 was taken at the 2013 central wavelength setting with the 0.1X0.03 aperture, while o4g002060 was taken at 2263 with the 31X0.05NDA. Four echelle orders between 2125 and 2155 Å are included in both observations. Uncertainties in the blaze function alignment at different central wavelength settings, and possible vignetting caused by the different locations of the orders on the detector in the two observations prevent an exact comparison, but when we reduce the 31X0.05NDA aperture observations of HD 39060 in the same way as for the HD 36285 data, these observations show good agreement for the extracted fluxes and suggest that any error in the background subtraction amounts to no more than 4% of the mean flux level. These observations also suggest that near this wavelength, the throughput of the 31X0.05DA slit is about 20% lower than its tabulated value.

2.2. HD 214993

HD 214993 (12 Lac) is a complex multi-mode β Cephei variable, with at least six distinct pulsational frequencies (Jerzykiewicz 1978) with periods between 0.095 and 0.236 days. The interaction of the different modes leads to considerable variation in both the amplitude of the pulsation and in observed profiles of absorbtion lines. Periods and amplitudes of these modes were measured by Mathias et $al.$ (1994) using the Si III triplet at 4553, 4568, and 4575 Å. He fit the velocity curves with a sum of sinusoidal functions, although this fit does not perfectly track the velocity curve, possibly due to significant non-linearities in the pulsation amplitudes.

Our 11 subexposures of this star spanned about 0.195 d, or about 1 full cycle of the largest amplitude mode (0.193 d). We measured velocity shifts for each of the individual sub-exposures by cross-correlating the data in order 99 ($\approx$ 2045–2080 Å) with our adopted synthetic spectrum for this star. The strong Zn II ISM line was excluded from this cross correlation. The measured velocities are plotted vs. observation time in Fig. 1.

The 14 year span between the Mathias *et al.* observations and our STIS data is much too long to allow us to predict the phases of individual modes. However, for illustrative purposes we have overplotted a velocity curve that adopts Mathias *et al.*'s mode frequencies, amplitudes, and system velocity, but with phases for the individual modes arbitrarily adjusted to fit our observed data. The rms residuals of this fit are only about 2 km s^{-1}.

In Fig. 2 we show for each subexposure the observed spectrum in echelle order 99. For our analysis we only used the data from subexposures 4, 5, and 6 which show the narrowest line profiles, which were taken when the star was near its maximum radius. We compare the coadded data for these subexposures to the coaddition of the other subexposures in Fig. 3. Note that the optical analysis of Gies & Lambert (1992) did not comment on the pulsational phase at which their observations were taken. This may introduce some additional uncertainties into their results for this star.

3. Abundance Analyses

Elemental abundances have been determined from LTE spectrum syntheses and ATLAS9 model atmospheres (Kurucz 1979, 1989). Solar metallicity models were used throughout. The stellar temperature and gravity values were adopted from the literature; see Table 3. For HD 36285, the temperature is from Cunha & Lambert (1994; CL94). For all other targets, temperatures are from Gies & Lambert (1992; GL92) scaled down by 3.4% to bring them into agreement with the CL94 temperature scale.

LTE spectrum syntheses were constructed using the program LINFOR[3]. The spectral line list covers the region from 2044 to 2145 Å, and was adopted from Brooks *et al.* (2002). This line list originated from the Kurucz (1993; CD-18) line list, including light elements, all lines in the iron-group, and heavy elements up to barium, and through the third ionization states. The line list was updated to include new wavelengths and/or oscillator strengths for $\sim$180 Fe III lines (Proffitt *et al.* 1999; Ekberg 1993). Brooks *et al.* also included some fine

---

[3]LINFOR was originally developed by H. Holweger, W. Steffen, and W. Steenbock at Kiel University. It has been upgraded and maintained by M. Lemke, with additional modifications by N. Przybilla

adjustments to iron-group features after an examination of the synthesis of their sharpest lined stars; this included 5 Mn III lines and 26 Fe III lines. The final linelist includes 6685 features, although many are negligible contributors. Atomic data for the B III $2s^2$S - $2p^2$P resonance doublet with lines at 2065.8 Å and 2067.3 Å are taken from Proffitt *et al.* (1999).

The weaker B III line at 2067.3 Å is blended with a strong Fe III line and weaker Mn III line, and is not suitable for boron abundance determinations. For all syntheses, an isotopic ratio of ^{11}B/^{10}B=4.0 is adopted, the solar system ratio (Zhai & Sahw 1994, Shima 1963) which is consistent with the values determined by Proffitt *et al.* (1999) from their line profile analysis of two sharp-lined B-type stars.

As discussed by Proffitt & Quigley (2001), interstellar (IS) lines must be addressed, particularly due to the capacity of one Cr II IS line at λ2065.50 to be shifted into a blend with the boron feature. All of our stars have been examined for IS lines. In no instance does an IS line interfere with the B III features. All four of the IS lines near the B III feature are only observable in one star, HD 22951 (see Fig. 4).

3.1. Spectrum Syntheses: I. Line by Line Analysis

For five of the seven targeted stars, the S/N of the reduced spectra and their broadening parameters (sharp lines) made it possible to identify and fit individual stellar features for a line-by-line analysis. The wavelengths and abundances from these (mostly iron-group) features are listed in Table 4. Abundance results are listed relative to meteoritic values from Asplund, Grevesse & Sauval (2005), with 12+log(Fe/H, Mn/H, Ni/H, Cr,H, Co/H) =(7.45, 5.47, 6.19, 5.64, 4.82). Not all iron-group features were used in the final iron-group abundances listed in Table 5; due to poor atomic data in the UV and/or unrecognized blends, we iterated such that the average value includes only features within 2σ of the mean.

Microturbulence values were calculated in this line-by-line analysis by requiring that iron-group abundances match for both strong and weak features (i.e., the features in Table 4 within 2σ of the mean). This analysis yields microturblence results significantly lower than ones determined using optical observations of these same stars (Gies & Lambert; 1992). This same trend has been noted by both Venn *et al.* (1996) and Cunha *et al.* (1997), and is likely a reflection of differences in the atmospheric structure between the formation of the UV and optical spectral regions. Macroturbulence was taken as the instrumental broadening (9 km s^{-1} for the E230M grating and 4 km s^{-1} for the E230H grating). Values for rotational broadening and radial velocities were calculated via line profile fitting for each star from the iron group features in Table 4. Spectrum syntheses in Fig. 4 show the best fit iron

abundance.

Boron abundances were determined from best fit syntheses of the $\lambda 2065.8$ B III line, even though it is blended with a weak Mn III line at $\lambda 2065.9$. The measurement of this Mn III line has been shown to be in good agreement with the overall iron-group abundance (Venn *et al.* 2002 = V02), thus the mean Fe group abundance was adopted for the Mn abundance prior to the boron abundance calculations. The best fit boron abundances, and syntheses with [B/H]=±0.4 dex, are shown in Fig. 4. The broadening parameters, and LTE iron-group and boron abundances are summarized in Table 5.

In this analyses, all of the target stars result in lower iron-group abundances than anticipated for objects in the Orion star forming region or the solar neighborhood. Cunha, Smith & Lambert (1998) examined F and G-type stars in the Orion complex and found iron abundances from optical observations of Fe I and Fe II lines that were consistent with other stars in the solar neighborhood (log(Fe/H)~ -0.1). The fact that our analysis of B-stars results in iron-group abundances that are sub-solar by [Fe/H] = 0.1 to 0.4 appears to be partially due to the temperatures adopted. In V02, boron and iron-group abundances were determined using temperatures from the literature. The boron abundances were then scaled to a common temperature scale, but not the iron-group abundances. If the iron-group abundances had also been scaled (e.g., reducing the Gies & Lambert 1992 temperatures by 3.4%, as done in this paper from the beginning), then those abundances would have been reduced by ~ 0.1 dex, in better agreement with the results in this paper. The iron-group abundances are also very sensitive to microturbulence for which there are very few constraints in our UV spectra. In V02, we showed that $\Delta \xi = \mp 1$ km s^{-1} results in Δ[Fe/H] $\sim \pm 0.20$. If all of the microturbulence values in this paper are reduced by 1 km s^{-1}(with no changes in temperature) then the mean iron-group abundance is solar. These changes in temperature and microturbulence have much smaller effects on boron, Δ[B/H] ≤ 0.05 and 0.02, respectively (see Section 4). Thus, we do not expect that the low iron-group abundances found here affect the main science in this paper, i.e., accurate boron abundances in B-type stars.

3.2. Spectrum Synthesis: II. Two Exceptions

Of the seven target stars, two had spectra that prevented a detailed line-by-line study. Because only three of the subexposures for HD 214993 could be used, this resulted in a lower signal-to-noise spectrum, while HD 30836 has very broad features due to its high $v\sin i$ value.

Lines that were determined to be "clean" in the high quality spectra (lines that do not deviate from the mean abundance by more that 2σ for the 5 stars discussed above in

Section 3.1, see Table 4) were used to find the rotational and radial velocities. Using these parameters, a best metallicity and microturbulence was determined simultaneously (where the metallicity range examined ranged from solar and 1/3 solar). The best-fit spectrum syntheses are shown in Fig. 5. In both cases, sub-solar metallicities were found to fit best (see Table 5). For HD 30836 and HD 214993 the best fit iron-group abundance was adopted for the Mn III abundance (blended with the boron line), and used to calculate the boron abundance or its upper limit (see Fig. 5).

3.3.   Spectrum Synthesis: III. HD35299

We have synthesised the Goddard High Resolution Spectrograph (GHRS) spectrum of HD 35299 near 2066Å from Proffitt *et al.* (1999; see also Lemke *et al.* 2000) to verify that our methods and models are consistent with previous analyses that found a solar boron abundance for this star. Temperature and gravity values are from CL94. Macroturbulence was set to the instrumental broadening, 3.5 km s^{-1}, as calculated using FWHM (0.0246 Å) from Proffitt *et al.*(1999). Rotational broadening (8 km s^{-1}), and radial velocities were calculated here via line profile fitting of the iron features deemed best in Table 4 (although the spectral range is smaller $\lambda\lambda$2059-2073). Microturbulence was taken as the best fit value for each of the input abundances. The HD 35299 spectrum is plotted in Fig. 6 and shows the best-fit iron-group (log(Fe/H)=7.20) and boron (log(B/H)$_{NLTE}$=2.55) abundance synthetic spectrum. For comparison, we also show the best-fit boron abundance ±0.4 dex. This iron-group abundance is consistent with the average of log(Fe/H)from the two "clean" (as described in Section 3.1) iron lines that fall into the wavelength range of our observations. This value was used to set the abundance of the Mn III blend at λ2065.9. This NLTE boron abundance is in good agreement with the results from both Proffitt *et al.* (log(B/H)=2.41)[4] and Lemke *et al.* (log(B/H)=2.70).

3.4.   Nitrogen and Oxygen Abundances

In Table 3, we have reduced the GL92 temperatures by 3.4% and applied their nitrogen and oxygen abundance corrections for this temperature change (the Δ values in their Table 9). We have also applied a correction to account for differences in the LTE abundances determined from their use of Gold as opposed to the more heavily line-blanketed Kurucz

---

[4]This value has been adjusted to the CL94 temperature scale and NLTE corrected using Table 8 from V02

model atmospheres. These corrections have been calculated by CL94 (their Table 10). Note that CL94's corrections are to the LTE abundances, and we assume that the same will apply to the NLTE abundances. For stars that have been studied only by CL94, similar corrections have been applied to account for the differences between LTE Gold and Kurucz model abundances.

4.   Boron and Iron-group Abundance Uncertainties

In this analysis, we have listed the line-to-line scatter in the iron-group abundances in Table 4. For all other iron-group uncertainties (atmospheric parameters, metallicities, spectral resolution, and S/N), we refer to Table 7 in V02 since their targets stars, UV spectra, and methodology are similar to those in this paper. Most of these atmospheric effects result in iron-group uncertainties ≤ 0.1 dex, with the exception of ξ which is larger (~ 0.20 dex). The macroturbulence and radial velocity measurements are estimated with uncertainties of ± 2 km s^{-1} based on the line profile fitting. Microturbulence is estimated as accurate to $\pm$ 1 km s^{-1} based on line strengths. Overall, the iron-group uncertainties are estimated as $\Delta \log(\mathrm{Fe/H}) = 0.25$ dex.

To determine the uncertainties in the boron abundances, we have used similar methods to those described in V02 and Brooks *et al.* 2002, calculating the offset in the boron abundance due to the uncertainties in temperature and gravity (as published), macroturbulence, microturbulence, and radial velocities (from our iron-group analysis), and location of the continuum ($\pm 1\%$). The abundance of the Mn III line blended with the B III line was maintained constant during the boron uncertainty calculations. Brooks *et al.* showed that the error determined when Mn remains fixed is in good agreement with that determined by refitting the Mn line with each successive error calculation. The resulting boron uncertainties are listed in Table 6; the total error for boron is taken as the sum of the squares of these values. As was found in Brooks *et al.*, the accuracy of the atmospheric parameters (temperature and gravity) is the greatest source of error in the boron abundance.

The isotopic ratio of ^{11}B/^{10}B can also have a small effect on the derived boron abundance. In V02, a ratio of 2.0 was found to change $\log(\mathrm{B/H})$ by ≤ 0.12 dex.

4.1.   The Lyubimkov *et al.* Temperature Scale

In addition to the uncertainties in the atmospheric parameters, we also calculated the errors if we adopt a different temperature scale. Lyubimkov *et al.* (2002) report cooler

temperatures for B-stars. The iron-group and boron abundances were calculated for five of our stars (those that underwent the line-by-line analyses) with temperatures and gravities from both Lyubimkov *et al.* and GL92-3.4%, and are compared in Table 7. Both the iron and boron abundances are lower by 0.02 to 0.26 dex using the Lyubimkov temperatures (and gravities). There is no obvious correlation between these corrections and temperature, unlike the results for oxygen from Daflon *et al.* (2004). The typical correction to the iron or boron abundances is ~ -0.1 dex, thus the change in temperature scale seems to have only a small effect on our abundance determinations.

We also note that for this test, four (out of the five) stars had values of T_{eff} and log g calculated directly by Lyubimkov *et al.*(2002). In order to correct the fifth star, HD 22951, equations 6 and 8 from Lyubimkov *et al.* were used to calculate the new T_{eff}. This choice of equations was based on a previous log g=4.4 determination for HD 22951. This new temperature was then used to estimate a new value for log g (from their Fig. 13). Values for $[c_1]$, Q, and β were obtained from Hauck & Mermilliod (1998). In order to confirm our methods, adjusted values of T_{eff} and log g were calculated for HD 35337 with the above described method and were found to be in excellent agreement with the values listed in Table 1 of Lyubimkov *et al.*(2002). We note this because the iron and boron abundance corrections for HD 22951 are the largest in Table 7.

5. Discussion

Current stellar evolution models that include rotation follow the evolution of the angular momentum distribution and associated mixing processes in massive stars from the pre-main sequence through core collapse. Rotational mixing can affect stellar surface abundances, stellar life times, and the evolution of a star across the HR diagram, thus stellar mass estimates. Generally, a rotating star has a lower effective gravity, thus it acts like it has less mass at core-H ignition. During core-H burning, rotationally induced mixing of protons from the envelope into the convective core and of helium from the core into the envelope will lead to higher luminosities compared to non-rotating models. Evolution on the main-sequence then depends on mass and rotation rate, as well as the efficiency of mixing in the upper convective core and stellar interior.

Stellar evolution models by Heger & Langer (2000) follow the changes in the surface abundances of boron and nitrogen as a function of time (age) for a variety of stellar masses (8 to 25 $M_\odot$) and initial rotation rates (0 to $\sim$450 km s^{-1}). These relationships are important because they show that boron is a much more sensitive indicator of mixing processes in B-type stars than the more commonly examined CNO abundances. Two sets of models

are computed by Heger & Langer, with different assumptions on the efficiency of rotational mixing in layers containing a gradient in the mean molecular weight μ (called a μ-barrier). The differences between the two sets of models reflects the remaining uncertainties in the theoretical description of the rotational mixing processes. It is interesting to note that even though the rotationally induced μ-barrier *inhibits* mixing just above the core, the current models show that the envelope above the μ-barrier is very well mixed, thus CN-processed gas is *more* evident up through the photosphere than when the μ-barrier is ignored. The models also show the degeneracies in the stellar abundances (CNO and boron) with mass, age, and rotation rate. Thus, determination of these stellar abundances *alone* cannot uniquely constrain rotational mixing scenarios; additional information (such as mass, rotational velocity, or age) of the target stars is necessary.

In this paper, we attempt to constrain both mass and age for our selection of stars while interpreting their CNO and boron abundances. Mass is constrained by the model atmosphere parameters; in Fig. 7, it is clear that most of our target stars are $\sim$12 M$_\odot$, ranging in mass from 8 to 14 M$_\odot$. Age is constrained by our initial selection of stars in young clusters[5], see Table 1. Unfortunately, the rotation rates themselves cannot be constrained because we are required to analyse sharp-lined stars for reliable boron determinations, which could be either slowly-rotating or nearly pole-on rapidly rotating stars. Abt, Levato, & Grosso's (2002) statistical survey of rotation rates of B-type stars in the Bright Star Catalogue found B0-2V stars with a mean $v\sin i$ value of 127 $\pm$8 km s^{-1}, and that the highest $v\sin i$ value is 410 km s^{-1}, though these are very rare stars (0.3% of the sample had $v\sin i \geq 350$km s^{-1}). This velocity range is covered by the Heger & Langer models. Nevertheless, with nearly all other parameters constrained, then we can compare the predictions from the evolution models for boron versus nitrogen *and* mass *and* age, for a range of rotation rates for our stellar sample.

5.1. Initial Abundances of Boron and Nitrogen

The meteoritic abundance of boron is adopted as the initial abundance of boron in the B-type stars in this paper, 12+log(B/H)= 2.78$\pm$0.04 (Zhai & Shaw, 1994). This value is in good agreement with the new 3D solar photospheric boron abundance determined by Asplund, Grevesse, & Sauval (2005), as 12+log(B/H) = 2.70$\pm$0.2, with corrections for departures from

---

[5]The cluster ages depend on isochrone fitting, which in turn depend on stellar evolution models. Standard stellar evolution models without rotation are usually adopted when cluster ages are determined. Rotational mixing could have an effect on the ages of clusters, but it is not clear what the effect on age would be. Isochrone fitting takes into account all main-sequence (turn off) stars, and these stars can be expected to display a variety of rotation rates.

LTE. Their solar nitrogen abundance is determined from 3D analyses of NI and NH features (the NI result includes a small correction for NLTE), resulting in 12+log(N/H) = 7.78 ±0.06, which is in good agreement with other stars in the solar neighborhood. Additionally, the interstellar boron abundance from B II 1362 Å resonance lines in diffuse clouds in the solar neighborhood has a lower limit of 12+log(B/H)≥ 2.4 (Howk, Sembach, & Savage 2000, where a lower limit is given since boron may be depleted onto interstellar grains). In this paper, we assume the solar abundances are representative of the stars in the solar neighborhood, even the younger B-type stars (even though one may ask why there has been so little chemical enrichment over the ∼5 Gyr lifetime of the Sun).

5.2. Boron versus Nitrogen: Predictions and Observations

In hot stars, the boron-nitrogen relationship is of particular interest because the majority of boron in the star is destroyed very early in its main-sequence lifetime ($\leq 10^4$ yr), leaving only the outermost layers to retain their initial boron abundance. Subsequent mixing of CN-cycled gas towards the surface of the star through convective overshoot and/or semi-convection results in a downward mixing of the boron rich outer layers toward the stellar interior. Because of the shallow mixing required for boron to be destroyed (only about 1 $M_\odot$ down), its depletion manifests itself prior to the CN-cycle nitrogen gas being mixed to the surface. Predictions for the change in boron versus nitrogen from the Heger & Langer (2000) models are shown in Fig. 8, where it can be seen that a clear signature of rotating models is that the reduction in boron is far greater than the increase in nitrogen. The dotted lines in Fig. 8 are from the same model (12 $M_\odot$, ZAMS V_{rot} = 200km s^{-1}, and including μ-barriers), but various initial boron and nitrogen abundances. Interestingly, the boron-to-nitrogen relationship shown in Fig. 8 is nearly independent of mass, rotation velocity, and age in the stellar models (see Fig. 12 in V02).

Fig. 8 also shows that that most of the observational data follows or exceeds the predicted trend. All filled data points in Fig. 8 are boron determinations from B III 2066. Only one star has a solar boron abundance as determined from the B III lines, HD 35299, thus we reanalysed it here (see Section 3.3) to verify our methods. All the other stars have boron results from the B III line below 12+log(B/H)=2.3. For the stars in this paper, lower boron abundances are to be expected since targets were selected to have weak B III lines from IUE spectra.

Those stars with larger boron depletions than predicted from models may indicate additional or more efficient mixing, but one of the major advantages of the data set in this paper is that the boron and nitrogen abundances have been determined for stars in clusters, thus

stars which also have age constraints. In Figs. 9 and 10, we show the nitrogen and boron abundances versus their stellar cluster ages, respectively. Ages are listed in Table 1. The models shown in Figs. 9 and 10 (and also Fig. 7) include rotational mixing and μ-barrier effects for several different stellar models across a span of rotational velocities (0-450 km s^{-1}) from 10 to 20 $M_\odot$ in order to illustrate the effects of these parameters on abundance.

The predicted trend of boron-depletion and nitrogen-enrichment lends itself to certain constraints in the ability to detect boron if nitrogen is enhanced and/or with age. For example, boron is nearly undetectable after a nitrogen enrichment of only 0.4 dex (based on Fig. 8). From Fig.s 9 and 10, for a 12 $M_\odot$ star with v$_{rot}$=400 km s^{-1}, this time scale is no more than 10 Myr. Thus, boron's sensitivity to early mixing is far greater than that of nitrogen.

In comparing the observational stellar abundances to the model predictions, the stellar data do show a large range in boron abundances, from $0.9 \geq 12+\log(B/H) \geq 2.9$. The stars with $12+\log(B/H) \geq 1.8$ (which comprises 3/4 of the sample) *do not show significant nitrogen enrichments*; see Figs. 8 and 9. This suggests a range of a factor of 10 in boron *without* nitrogen enrichments, as predicted by stellar evolution models that include rotation. The remaining 1/4 of the sample, with $12+\log(B/H) \leq 1.8$, show a large range in nitrogen, some with no enrichments at all, i.e., HD 36591 and HD 30836. These two stars are discussed, independently, below.

In Fig. 10 most of the stellar data is in good agreement with the model predictions (for $\sim$12 M$_\odot$ stars, and given the uncertainty in the rotation rates). Only two stars stand out, HD 36591 and HD 205021, because their ages are so young and boron abundances so low. For HD 36591, its young age and low boron abundance suggests a 20 $M_\odot$ model with the fastest rotation rate (450 km s^{-1}); see Fig. 10. On the other hand, examination of Fig. 9 suggests a 15 M$_\odot$ model with the fastest rotation rate. However, its spectroscopic mass (from Fig. 7) is at most 13 $M_\odot$. In order for the masses to agree, the temperature needs to be increased by $\sim$15-30%. This result suggests that rotational mixing may be more efficient than currently modelled, at least at the highest rotation rates, and that the current models do not simultaneously predict the boron abundance, nitrogen abundance, mass, and age for this star.

The remaining two stars in our sample that stand out in either Fig. 8 or Fig. 10 are HD 30836 and HD 205021. Both are severely depleted in boron, but have also been identified as spectroscopic binaries. Binary mass transfer is another way of depleting surface boron abundances (Wellstein 2001; Langer, Wellstein, & Heger 2001). These stars have similar masses (10-12$M_\odot$ from Fig. 7) and orbital periods (10 days, Koch 1990). Models from Wellstein (2001) predict that mass transfer occurs in these systems shortly after core hydrogen

burning in the primary star. While binary mass transfer can produce boron depletions, only rotational mixing predicts boron depletion *without* nitrogen enrichments. HD 205021 shows a nitrogen enrichment (log(N/H) =8.0) in addition to its depleted boron abundance. We notice in Fig. 9 that the nitrogen enrichment and age for this star implies a mass of ∼20 $M_\odot$ and the highest rotation rate (450 km s^{-1}). The same result is found examining its low boron abundance and age in Fig. 10. However, its spectroscopic mass is only ∼12 $M_\odot$ (Fig. 7). Thus this star does not match the rotating model predictions, but could be affected by binary mass transfer.

HD 30836 shows no nitrogen enrichment (log(N/H)=7.79; Table 3), thus rotational mixing *uniquely* describes its abundance pattern. Ironically, we only have an upper-limit to the boron abundance in HD 30836, however that upper-limit is extremely low. We also only have an upper-limit to its age from membership in the Orion OB1 association (the sub-association is unclear for this star). From the rotating models, the upper-limit age and upper-limit boron abundance suggest that HD 30836 has a mass of 12 $M_\odot$ with a rotational velocity between 200 and 300 km s^{-1}(see Fig. 10). However, the spectroscopic mass (see Fig. 7) for this star is closer to 10 $M_\odot$. Adopting 10 $M_\odot$ in Fig. 10 would require a rotational velocity over 450 km s^{-1}, higher than the theoretical upper limit. Similarly, adopting a 12 $M_\odot$ in Fig. 7 would require an increase of nearly 3000 K (approximatly 15%) in temperature. Thus, the nitrogen abundance and upper-limits to age and boron abundance make HD 30836 another interesting star for comparing with the rotating stellar models, regardless of its binarity. This star, along with HD 36951 (and possibly HD 205021) are best fit by models with masses significantly larger than their spectroscopic masses. This suggests that rotational mixing is more efficient than currently modelled at the highest rotation rates.

6. Conclusions

Detailed abundances of boron have been determined in a careful selection of seven sharp-lined B-stars in young clusters to test massive star evolution scenarios that include rotational mixing effects. The seven stars in this analysis show moderate-to-severe depletions of boron (1/4 to 1/50 solar!) *without* significant nitrogen enrichments. This is a unique prediction of the massive star evolution models that include rotational mixing (Heger & Langer 2000), because shallow mixing will destroy surface boron abundances before deep mixing bring CN-cycled gas to the surface. Only three stars deviate from the model predictions, HD 30836, HD 36591, and HD 205021. In all three cases, their spectroscopic masses are smaller than predicted from the rotating evolution models (i.e., the masses required to explain their low boron abundances and young ages). These three stars appear to indicate that rotational

mixing is more efficient than currently modelled at the highest rotation rates. These results are consistent with previously published results (Venn *et al.* 2002), but approximately doubles the sample size of stars with both moderate and severe boron depletions.

REFERENCES

Abt, H. A., Cardona, O. 1984, ApJ, 285, 190

Abt, H. A., Levato, H., Grosso, M., 2002, ApJ, 573, 359

Asplund, M., Grevesse, N., Sauval, A. J. 2005, in ASP Conf. Ser. 336, Cosmic Abundances as Records of Stellar Evolution and Nucleosynthesis, ed. F. N. Bash, T. G. Barnes III (San Francisco: ASP), 25

Batten, A. H., Fletcher, J. M., Mann, P. J. 1978, PDAO, 15, 121

Boesgaard, A. M., & Lavery, R. J. 1986, ApJ, 309, 762

Brooks, A. M., Venn, K. A., Lambert, D. L., Lemke, M., Cunha, K., & Smith, V. V. 2002, ApJ, 573, 584

Brown, A. G. A., de Geus, E. J., & de Zeeuw, P. T. 1994, A&A, 289, 101

Cunha, K., & Lambert, D. L. 1994, ApJ, 426, 170 (CL94)

Cunha, K., Lambert, D. L., Lemke, M., Gies, D. R., & Roberts, L. C. 1997, ApJ, 478, 211

Cunha, K., Smith, V. V., & Lambert, D. L. 1998, ApJ, 493, 195

de Zeeuw, P. T., Brand, J. 1985, in ASSL vol. 120, Birth and Evolution of Massive Stars and Stellar Groups, Boland W., van Woerden, H., (Dordrecht: D. Reidel Publishing Co.), 95

Daflon, S., Cunha, K., Butler, K., 2004, ApJ, 604, 362

Dennisenkov, P. A., 1994, A&A, 287, 113

Eckberg, J. O., 1993, A&AS, 101, 1

Evans, C. J., Smartt, S. J., *et al.*, 2005, A&A, 437, 467

Fliegner, J., Langer, N., Venn, K.A., 1996, A&A, 308, 13

Gies,. D. R., & Lambert, D. L. 1992, ApJ, 387, 673 (=GL92)

Gold, M. 1984, Ph.D. thesis, Univ. München

Hauck, B., Mermilliod, M. 1998, A&AS, 129, 433

Heger, A., & Langer, N. 2000, ApJ, 544, 1016

Herrero, A., Kudritzki, R. P., Vilchez, J. M., Kunze, D., Butler, K., Haser, S. 1992, A&A, 262, 209

Howk, J. C., Sembach, K. R., & Savage, B. D. 2000, ApJ, 543, 278

Jerzykiewicz, M. 1978, Acta Astron., 28, 465

Klochkova, V. G., Kopylov, I. M. 1985, AISAO, 20, 3

Koch, R. H., 1990, Bull Inf. Centre Donnees Stellaires, 38, 175

Kurucz, R. L. 1979, ApJS, 40, 1

Kurucz, R. L. 1989, in Highlights of Astronomy 8, ed. D. McNally (Dordrecht: Kluwer), 168

Kurucz, R. L. 1993, CD-ROM 18, SYNTHE Spectrum Synthesis Programs and Line Data (Cambridge: SAO)

Lemke, M., Cunha, K., & Lambert, D. L. 2000, in 35th Liege International Astrophysics Colloq, The Galactic Halo: From Globular Cluster to Field Stars, ed. A. Noels, P. Magain, D. Caro, E. Jehin, G. Parmentier, & A. A. Thoul (Liege: Institut d'Astrophysique et de Geophysique), 223

Lindroos, K. P. 1986, A&A, 156, 223

Lyubimkov, L. S., Rachkovskaya, T. M., Rostopchin, S. I., & Lambert, D. L. 2002, MNRAS, 333, 9

Lyubimkov, L.S., 1996 $Astroph. SpaceSci.$, 243, 329

Maeder, A., & Meynet, G. 2000, A&A, 361, 159

Maeder, A., & Meynet, G. 2005, in ASP Conf. Ser. 337, The Nature and Evolution of Disks around Hot Stars, eds. R. Ignace, K. G. Gayley (San Francisco :ASP), 15

Mathias, P., Aerts, C., Gillet, D., Waelkens, C. 1994, A&A, 289, 857

Morrel, N., Levato, H. 1991, ApJS, 75, 965

Petrova, A. V., Orlov, V. V. 1999, AJ, 117, 587

Pinsonneault, M.H. 1997, ARAA, 35, 557

Proffitt, C. R., Jönsson, P., Litzén, U., Pickering, J. C., & Wahlgren, G. M. 1999, ApJ, 516, 342

Proffitt, C. R., & Quigley, M. F. 2001, ApJ, 548, 429

Roberge, A., Feldman, P.D., Lagrange, A.M., Vidal-Madjar, A., Ferlet, R., Jolly, A., Lemaire, J.L., Rostas, F., 2000, ApJ, 538, 904

Shima, M. 1963, Geochim. Cosmochim. Acta, 27, 991

Struve, O. 1951, ApJ, 113, 589

Venn, K. A., Brooks, A. M., Lambert, D. L., Lemke, M., Langer, N., Lennon, D. J., & Keenan, F. P. 2002, ApJ, 565, 571 (=V02)

Venn, K. A., Lambert, D. L., Lemke, M., 1996, A&A, 307, 849

Wellstein, S. 2001, Ph.D. thesis. Univ. Potsdam

Wellstein, S., Langer, N., & Braun, H. 2001, A&A, 369, 939

Zhai, M., & Shaw, D. M. 1994, Meteoritics, 29, 607

Table 1.   Basic Parameters

Star	Name	Sp. Type	Variable	Binary	OB Assoc.	Assoc. Age (Myr)	Ref.
HD 22951	o Per	B0.5V	$\cdots$	Visual? (check)	Per 0B2	12-20	1,3,4
HD 30836	π^4 Ori	B2III	$\cdots$	Spect.	Ori OB1	$\leq$11.4	2,5,6
HD 34816	λ Lep	B0.5IV	$\cdots$	$\cdots$	Ori OB1	$\leq$11.4	2
HD 35337	8 Lep	B2IV	$\cdots$	$\cdots$	Ori OB1c	$4.6^{+1.8}_{-2.1}$	2,6
HD 36285	$\cdots$	B2IV-V	$\cdots$	$\cdots$	Ori OB1c	$4.6^{+1.8}_{-2.1}$	2,6
HD 36960	$\cdots$	B0.5V	Variable?	Visual	Ori OB1c	$4.6^{+1.8}_{-2.1}$	2,7,8
HD 214993	12 Lac	B2III	β Cep	$\cdots$	Lac OB1	6-8	1,9

References. — (1)de Zeeuw & Brand 1985 (2)Brown, de Geus, & de Zeeuw 1994 (3)Klockova & Kopylov 1985 (4)Petrova & Orlov 1999 (5)Batten, Fletcher, & Mann 1978 (6)Abt & Cardona 1984 (7)Morrell & Levato 1991 (8)Lindroos 1986 (9)Struve 1951

Table 2.   HST STIS Observing Information for Galactic B-stars

Star	V	Grat/Slit	Exposure(s)	Date	S/N
HD 22951	4.98	E230M 0.2x0.05ND	1707 at λ_c2124 2634 at λ_c2124 2773 at λ_c1978 2760 at λ_c2269	2003 Mar 25	50
HD 30836	3.67	E230M 0.2x0.05ND	856 at λ_c2124 720 at λ_c2124 1200 at λ_c1978 1091 at λ_c2269 720 at λ_c2124 600 at λ_c2124 1200 at λ_c1978 1200 at λ_c2269	2003 Apr 6 2003 Aug 2	65
HD 34816	4.27	E230M 0.2x0.05ND	855 at λ_c2124 720 at λ_c2124 1200 at λ_c1978 1091 at λ_c2269	2003 Apr 25	80
HD 35337	5.22	E230M 0.2x0.05ND	3036 at λ_c2124 2166 at λ_c1978 1347 at λ_c2269	2003 Apr 24	100
HD 36285	6.32	E230H 31x.0.05NDA	572 at λ_c2013 1080 at λ_c2013 1260 at λ_c2013 1272 at λ_c2013 1200 at λ_c2013 624 at λ_c2013 1410 at λ_c2013 1410 at λ_c2013 1410 at λ_c2013 1388 at λ_c2013	2003 Apr 28	280
HD 36960	4.78	E230M 0.2x0.05ND	1661 at λ_c2124 1560 at λ_c1978 720 at λ_c2269	2003 Apr 27	90
HD 214993	5.23	E230M 0.2x0.05ND	2160 at λ_c2124 2640 at λ_c1978 1800 at λ_c2269	2003 Jul 7 2003 Jul 8	40

Table 3.   Stellar Parameters from Literature

Star	GL92-3.4% T_{eff} (K)	CL94 T_{eff} (K)	log g	NLTE log(N/H)	NLTE log(O/H)	Corrected log(N/H)	Corrected log(O/H)
HD 22951	27870	$\cdots$	4.40	7.69	8.45	7.69	8.42
HD 30836	21370	$\cdots$	3.60	7.79	$\cdots$	7.75	$\cdots$
HD 34816	28870	$\cdots$	4.20	7.66	8.75	7.59	8.67
HD 35337	23590	$\cdots$	4.20	7.65	8.56	7.64	8.55
HD 36285	$\cdots$	21930	4.40	7.77	8.79	7.77	8.55
HD 36960	28940	28920	4.30	7.72	8.88	7.65	8.80
HD 214993	24760	$\cdots$	4.00	7.80	8.78	7.82	8.83

Note. — Corrections made to the nitrogen and oxygen abundances are based on both the reduced GL92 temperature scale and an adjustment from the less heavily line-blanketed Gold models to those of Kurucz, as discussed by CL94. Adjustments are made according to the errors found in Table 9 of GL92 (Δ values) and Table 10 of CL94.

Table 4.   Iron-group Abundance Results

λ (Å)	Element(s)	[M/H] HD 22951	[M/H] HD 34816	[M/H] HD 35337	[M/H] HD 36285	M/H HD 36960
2048.92.....	Mn III	*+0.26*	-0.09	+0.13	-0.04	-0.06
2049.37.....	Fe III+Mn III	-0.20	*+0.00*	-0.08	-0.05	-0.10
2049.66.....	Mn III	-0.51	-0.43	*+0.38*	*+0.16*	-0.31
2050.74.....	Fe III	*-0.90*	-0.25	+0.01	-0.35	-0.12
2051.85.....	Fe III+Fe IV	*-0.05*	-0.15	-0.09	-0.10	-0.15
2052.27...	Fe III	-0.60	-0.41	-0.17	-0.35	-0.27
2053.52.....	Fe III	*-1.00*	*-0.71*	*-0.43*	-0.38	*-0.45*
2054.56...	Fe IIIx3	-0.37	-0.23	-0.13	-0.04	-0.10
2055.86.....	Fe III	-0.17	*+0.02*	+0.03	-0.21	*+0.14*
2056.16.....	Fe III	-0.59	*+0.13*	-0.20	-0.25	*+0.15*
2057.07.....	Fe III	-0.54	*0.00*	-0.22	*-0.46*	*+0.25*
2057.93...	Fe III	-0.49	-0.10	-0.27	-0.40	-0.09
2058.21.....	Fe III	*-0.11*	*+0.15*	-0.05	-0.08	*+0.25*
2058.57.....	Fe III	-0.35	*+0.35*	*+0.17*	-0.10	*+0.35*
2059.67.....	Fe III	*-0.82*	*+0.07*	*+0.15*	-0.20	-0.01
2063.40.....	Mn III	-0.42	-0.54	*+0.16*	-0.14	-0.34
2066.40...	Mn IIIx2+Ni III	-0.54	-0.54	-0.14	-0.28	-0.39
2068.26.....	Fe III	-0.57	*+0.38*	*+0.25*	*+0.05*	*+0.38*
2068.99.....	Fe III+Mn III+Cr III	-0.70	*-0.70*	-0.10	-0.05	*-0.50*
2069.82...	Fe III+Mn III	-0.20	-0.20	-0.09	-0.09	-0.15
2070.56.....	Fe III	-0.40	*+0.08*	-0.14	-0.36	*+0.15*
2070.98.....	Fe IIIx3	-0.55	-0.48	*-0.32*	-0.32	-0.33
2073.35...	Fe III+Mn III	-0.30	-0.28	-0.05	-0.13	-0.30
2074.23.....	Fe III	-0.62	*-0.65*	*-0.32*	*-0.55*	-0.40
2076.32.....	Fe III	-0.63	*-0.74*	-0.05	*-0.50*	*-0.72*
2077.36...	Mn III+Co III	-0.23	-0.53	+0.04	-0.13	-0.33
2077.74.....	Fe III+Fe IV	*+0.12*	*+0.10*	*+0.15*	*+0.01*	*+0.10*
2078.08.....	Fe III+Mn III	-0.30	-0.40	*-0.43*	*-0.50*	-0.43
2079.00.....	Fe IIIx4	-0.60	*+0.25*	+0.09	-0.45	*+0.20*
2080.22...	Fe III	-0.30	-0.38	-0.10	-0.25	-0.29
2081.08...	Mn IIIx2+Co III	-0.25	-0.13	-0.06	-0.28	-0.23
2082.38...	Fe III	-0.25	-0.35	+0.00	-0.10	-0.36
2083.55...	Fe III	-0.20	-0.20	+0.05	-0.25	-0.07
2084.36.....	Fe IIIx3+Mn IIIx2	-0.60	-0.43	-0.15	*-0.65*	-0.37
2084.93.....	Fe IIIx2	-0.40	-0.30	*+0.15*	-0.20	-0.15
2085.84...	Fe III+Cr III	-0.25	-0.15	+0.02	-0.14	-0.15

Table 4—Continued

λ (Å)	Element(s)	[M/H] HD 22951	[M/H] HD 34816	[M/H] HD 35337	[M/H] HD 36285	M/H] HD 36960
2087.15.....	Fe III	*-1.05*	-0.31	+0.10	-0.37	-0.38
2087.93.....	Fe III	*-0.80*	-0.51	+0.13	-0.40	-0.44
2089.12...	Fe III	-0.65	-0.03	+0.01	-0.45	+0.02
2090.16.....	Fe IIIx4+Mn IIIx3	*-1.10*	-0.45	+0.05	-0.15	*-0.45*
2091.35.....	Fe IIIx2	-0.65	-0.46	*-0.32*	*-0.48*	-0.40
2092.97.....	Fe III	-0.20	*+0.00*	-0.05	-0.22	*+0.15*
2093.51.....	Fe III	-0.25	*-0.58*	-0.08	-0.25	-0.13
2095.66.....	Fe IIIx3	-0.25	-0.44	-0.15	-0.05	-0.20
2096.42.....	Fe III	-0.60	-0.40	-0.14	-0.23	-0.05
2099.30.....	Fe IIIx2	-0.50	*-0.55*	-0.15	-0.45	-0.42
2101.04...	Fe III+Mn III	-0.50	-0.30	-0.07	-0.18	-0.20
2103.74.....	Fe IIIx4	*-1.00*	-0.48	*-0.40*	*-0.60*	-0.39
2104.96.....	Fe IIIx2+Cr III+Ni III	-0.32	-0.20	*+0.15*	*+0.03*	-0.18
2105.59.....	Cr III	*-0.15*	-0.19	-0.12	-0.10	-0.22
2107.34.....	Fe III	-0.45	-0.20	*-0.36*	-0.40	+0.00
2108.64...	Fe III+Mn III	-0.42	-0.43	-0.05	-0.07	-0.30
2111.80.....	Fe IIIx2	-0.30	-0.50	*-0.43*	-0.45	-0.43
2113.34.....	Fe IIIx2+Mn III	*+0.00*	-0.50	-0.04	-0.30	-0.18
2113.83...	Fe IIIx2+Cr III	-0.40	-0.35	+0.02	-0.23	-0.10
2114.34.....	Fe IIIx2+Cr III	*-0.15*	-0.25	+0.00	-0.11	-0.10
2114.88.....	Cr IIIx2	*-0.10*	*+0.00*	*+0.06*	-0.05	*+0.08*
2116.59.....	Fe IIIx2	*-0.95*	*-0.86*	+0.07	*-0.48*	*-0.72*
2117.55...	Cr III	-0.20	-0.27	-0.14	-0.20	-0.02
2118.49...	Fe IIIx2+Cr III	-0.45	-0.40	-0.05	-0.25	-0.30
2120.77...	Fe IIIx4+Fe IV	-0.53	-0.20	-0.07	-0.07	-0.15
2123.59...	Fe IIIx3+Cr III	-0.50	-0.40	-0.02	-0.05	-0.27
2124.16.....	Fe IIIx5+Co III	*-0.80*	*-0.70*	*-0.40*	-0.31	*-0.65*
2125.18.....	Fe IIIx5+Fe IV+Mn III	-0.55	-0.45	*-0.39*	-0.33	-0.35
2126.14...	Mn III	-0.28	-0.43	+0.00	-0.04	-0.39
2129.68...	Fe IIIx3	-0.20	-0.27	-0.08	-0.04	-0.23
2134.83.....	Fe IIIx2	*-0.08*	-0.04	*+0.29*	*+0.03*	*+0.12*
2136.36.....	Fe IIIx2	-0.56	*-0.74*	*-0.49*	*-0.65*	*-0.65*
Average....		-0.42	-0.33	-0.07	-0.22	-0.23
1 σ...........		+0.15	+0.16	+0.15	+0.14	+0.15

Note. — Results that fall $\geq 2\sigma$ from the mean are *italicized* and not included in the final average or 1 σ values. Wavelengths in **bold** are those that show consistent results across all five stars (none fall outside 2σ).

Table 5.   Atmospheric Analysis Results

Star	$v \sin i$ km s^{-1}	ξ km s^{-1}	log(Fe/H)	LTE log(B/H)	NLTE[1] log(B/H)
HD 22951	23	1	7.03±0.10	2.01±0.12	2.01
HD 30836	43	4	7.25±0.25	<1.2	<1.0
HD 34816	35	3	7.12±0.11	2.17±0.13	2.17
HD 35337	15	1	7.38±0.10	2.21±0.12	2.11
HD 36285	10	2	7.23±0.09	2.02±0.15	1.82
HD 36960	33	3	7.22±0.10	1.81±0.16	1.81
HD 214993	39	5	7.25±0.25	2.2±0.2	2.1

Note. — Macroturbulence values were set by the instrumental broadening; 9 and 4 km s^{-1}for observations with the E230M and E230H gratings, respectively.

[1]NLTE corrections were mading according to the grid used in V02 (their Fig. 9)

Table 6.   Boron Abundance Uncertainties

Parameters	HD22951 Δlog(B/H))	HD34816 Δlog(B/H)	HD35337 Δlog(B/H)	HD36285 Δlog(B/H)	HD36960 Δlog(B/H)
$\Delta T_{eff} = \pm 750$ K	±0.07	±0.07	±0.06	∓0.05	±0.12
$\Delta \log g = \pm 0.2$	±0.08	±0.07	±0.10	±0.13	±0.04
$\Delta \xi = \pm 1$ km s^{-1}	∓0.01	∓0.03	∓0.02	∓0.02	∓0.01
$\Delta \xi_{ma} = \pm 2$ km s^{-1}	±0.00	±0.02	±0.00	±0.00	±0.00
Shift continuum ± 1%	∓0.05	∓0.08	∓0.03	∓0.04	∓0.09
$\Delta V_{rad} = \pm 2$ km s^{-1}	±0.00	±0.01	±0.02	±0.02	±0.01
Total Error[1]	±0.12	±0.13	±0.12	±0.15	±0.16

[1]Total error is taken as the sum of squares of all of the uncertainties.

Table 7.   Atmospheric Parameters from Lyubimkov $et\ al.$ (2002)

Star	Lyubimkov02 T_{eff} log g	Δ [Fe/H]	Δ [B/H]
HD 22951	26300 4.00	0.26	0.18
HD 34816	27900 4.20	0.10	0.11
HD 35337	22300 4.00	0.12	0.06
HD 36285	21300 4.25	0.02	0.05
HD 36960	27500 4.15	0.15	0.13

Note. — $\Delta = \log(\mathrm{X/H})_{adopted}$ - $\log(\mathrm{X/H})_{L02}$
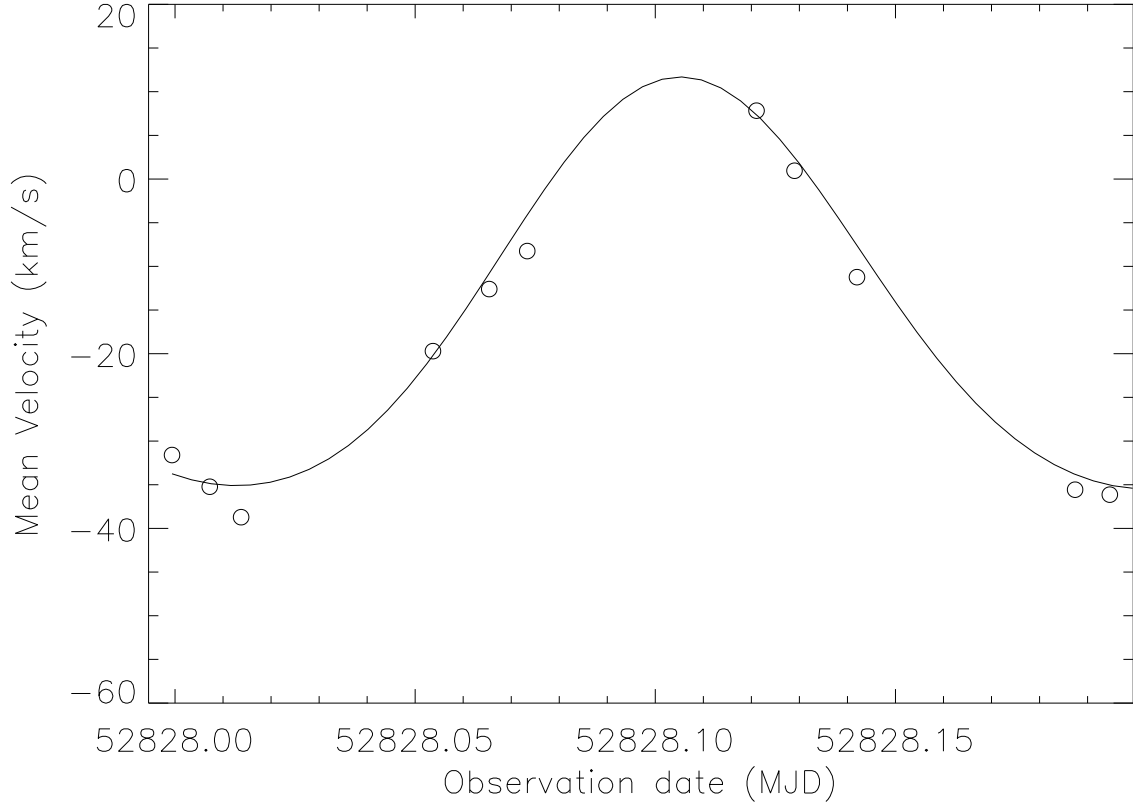
Fig. 1.— Measured radial velocity of each STIS subexposure of the β-Cephei star 12 Lac (HD 214993) is plotted as a function of the obervation start time. We have overplotted a velocity curve that adopts the pulsational frequencies and amplitudes found Mathias *et al.* (1994), but have adjusted the phases of each of the six pulsation modes to optimize the fit.
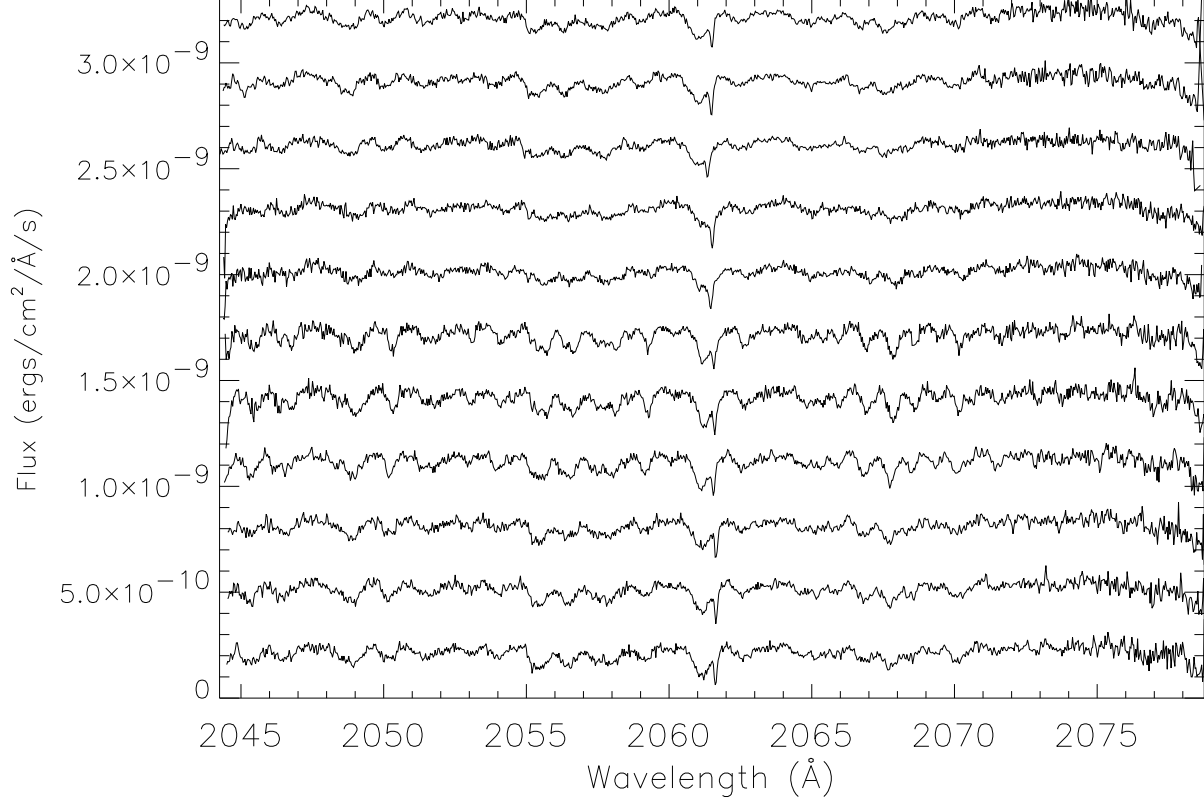
Fig. 2.— We show the individual spectra from order 99 of the STIS E230M grating for each individual subexposure of 12 Lac (HD 214993). The first subexposure is plotted at the bottom of the figure, and each of the subsequent spectra is offset by 3×10^{-10} flux units. The spectra are aligned to the laboratory wavelength scale in air.
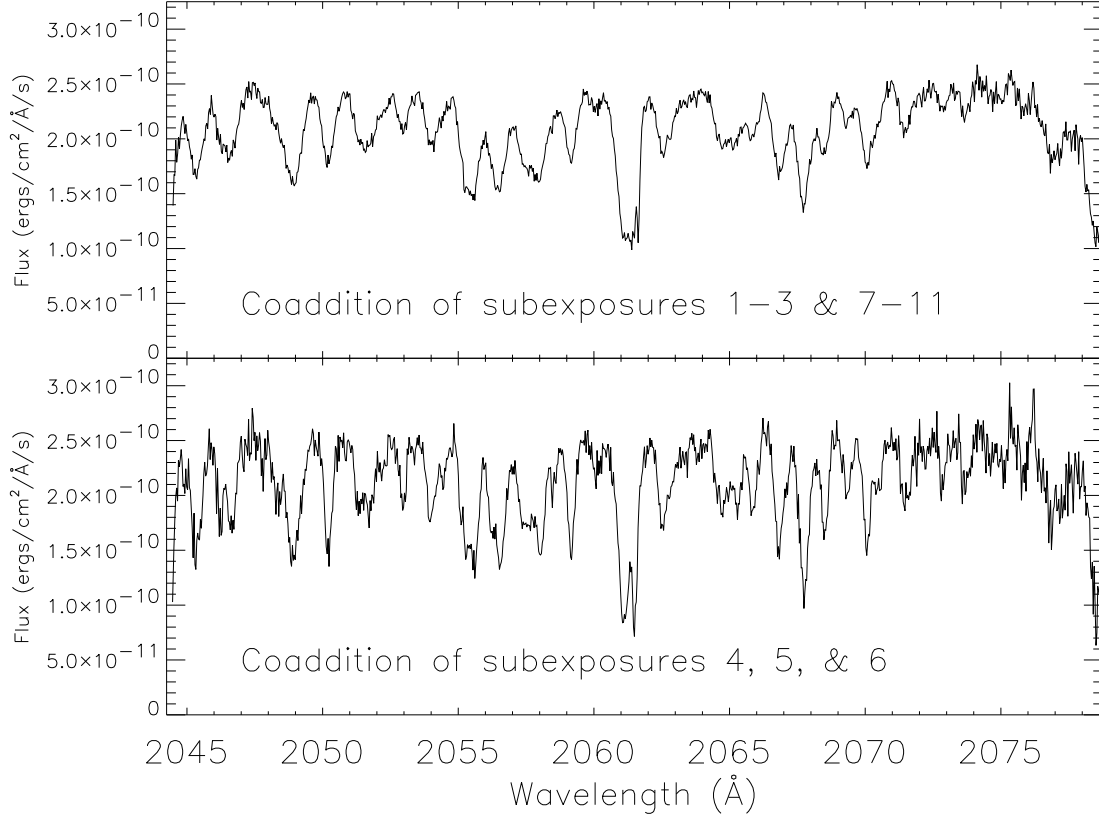
Fig. 3.— Coadded spectra for the three most narrow-lined observations of 12 Lac (bottom panel) are compared to the coaddition of the data for other phases. Each subexposure was shifted to the laboratory wavelength scale before coadding. Wavelengths are given in air.
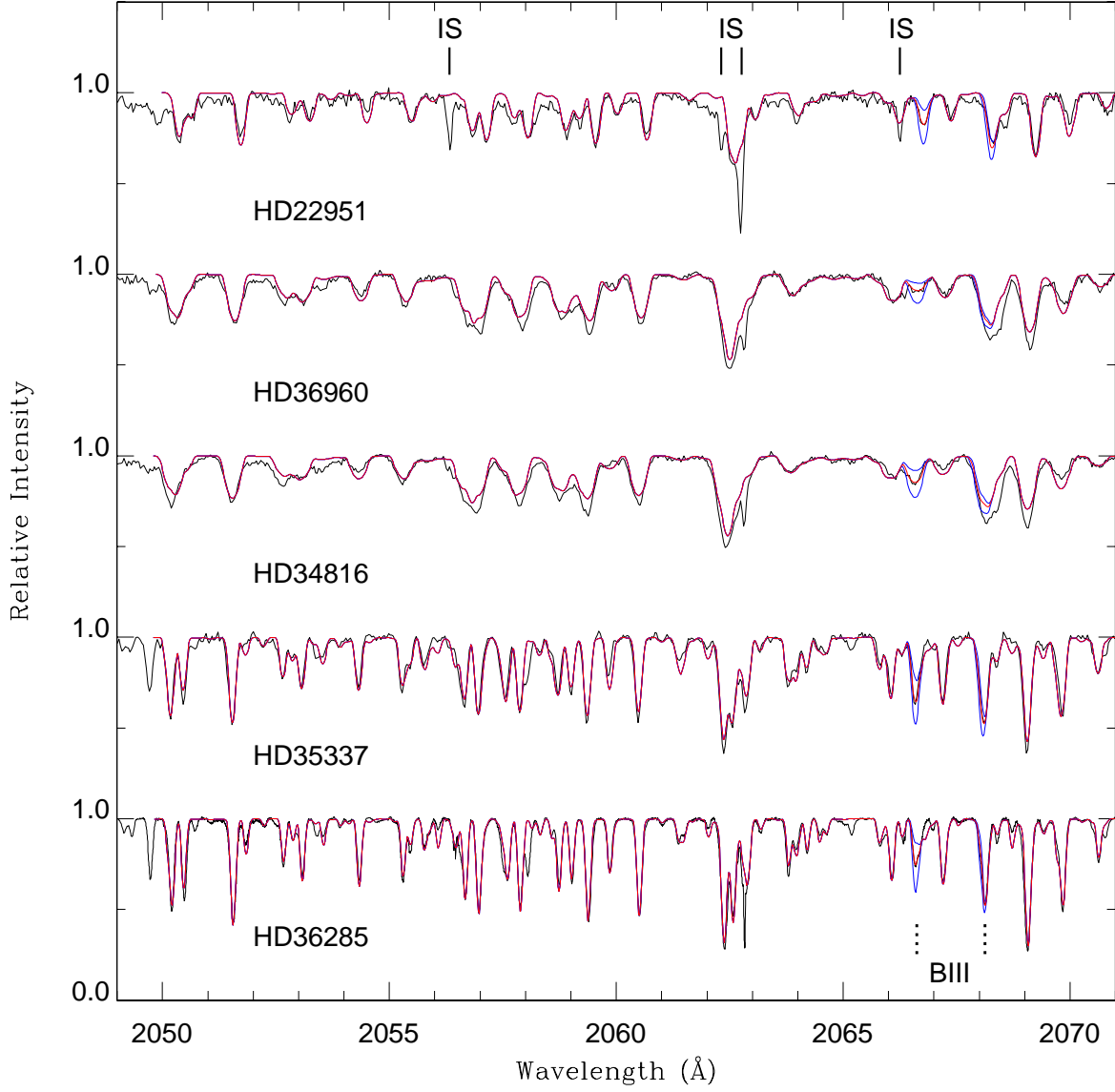
Fig. 4.— Best-fit metallicites and boron abundances (red) are compared to the spectra of five stars (black) with sufficiently high signal-to-noise spectra for a line-by-line analysis. Best-fit boron abundances ±0.40 dex are shown (blue) for comparison. Four interstellar lines are marked above the figures, while the boron lines are indicated below.
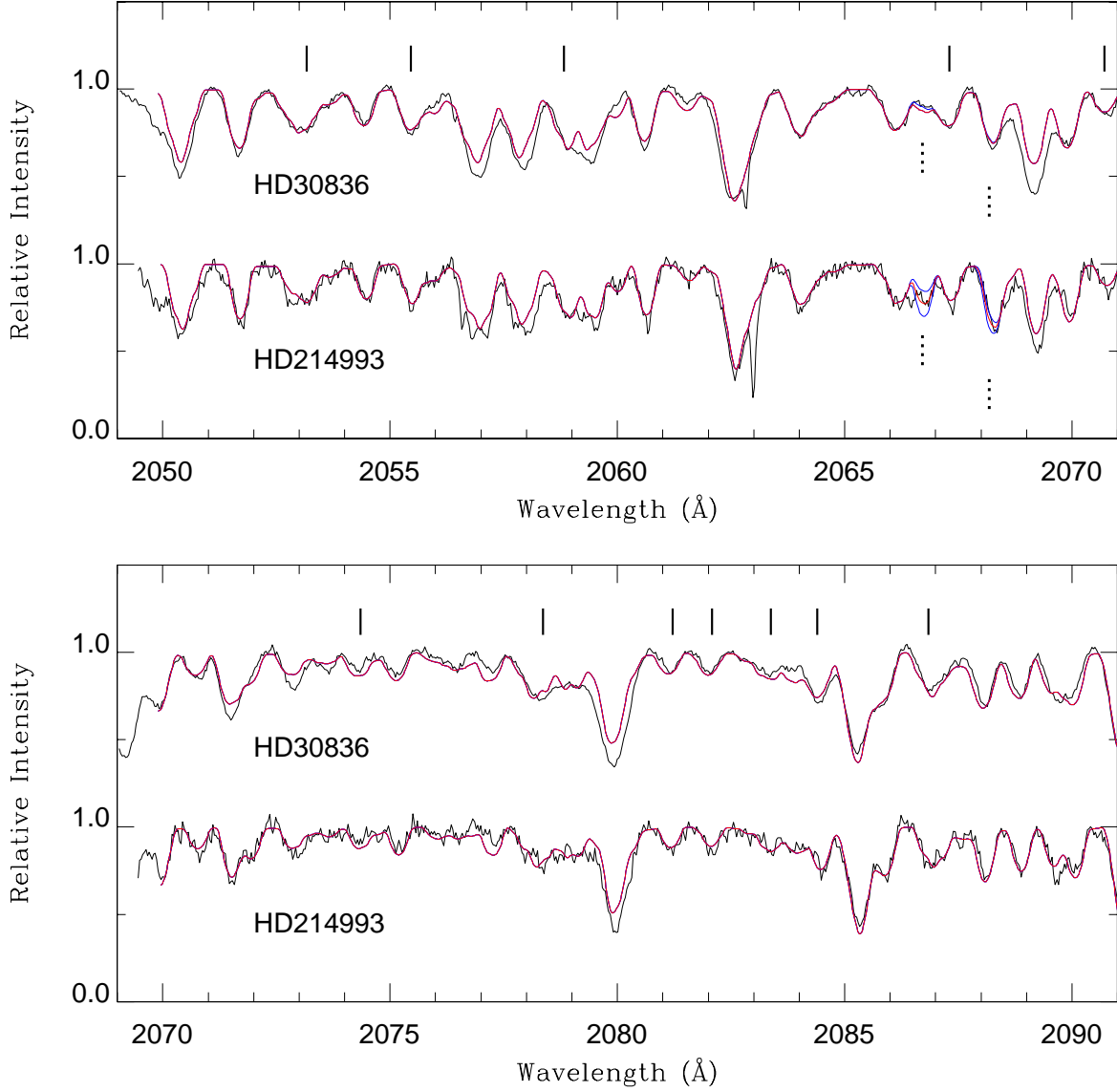
Fig. 5.— Best-fit metallicities and boron abundances (red) are compared to the spectra of two stars (black) with either lower signal-to-noise spectra (HD 214993) or lower gravity (HD 30836) than the other stars in this program. Best-fit boron abundances ±0.40 dex are shown (blue) for comparison, which also emphasizes the upper-limit determination for HD 30836. Rotational and radial velocities were determined from the most reliable iron-group lines (in Table 4 and marked above the spectra). Boron is indicated below the plots by the dotted lines.
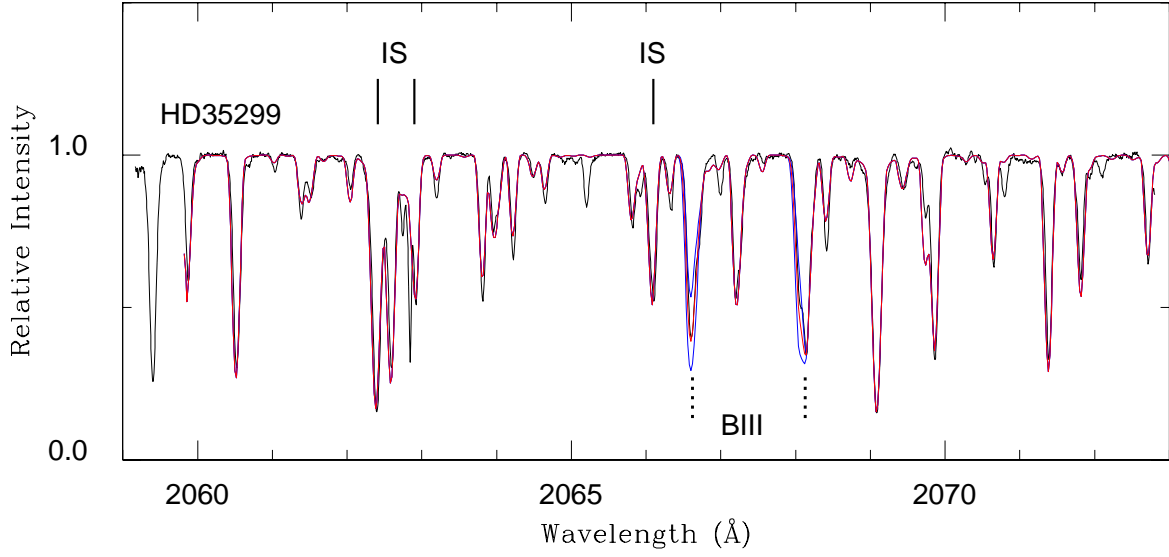
Fig. 6.— The HST-GHRS spectrum of HD 35299 (black; Proffitt *et al.* 1999) with best fit iron-group (log(Fe/H)=7.20) and boron (log(B/H)=2.55) spectrum synthesis (red). Best-fit boron ±0.40 dex is also shown (blue). We use this star to check our methods (see Section 3.3).
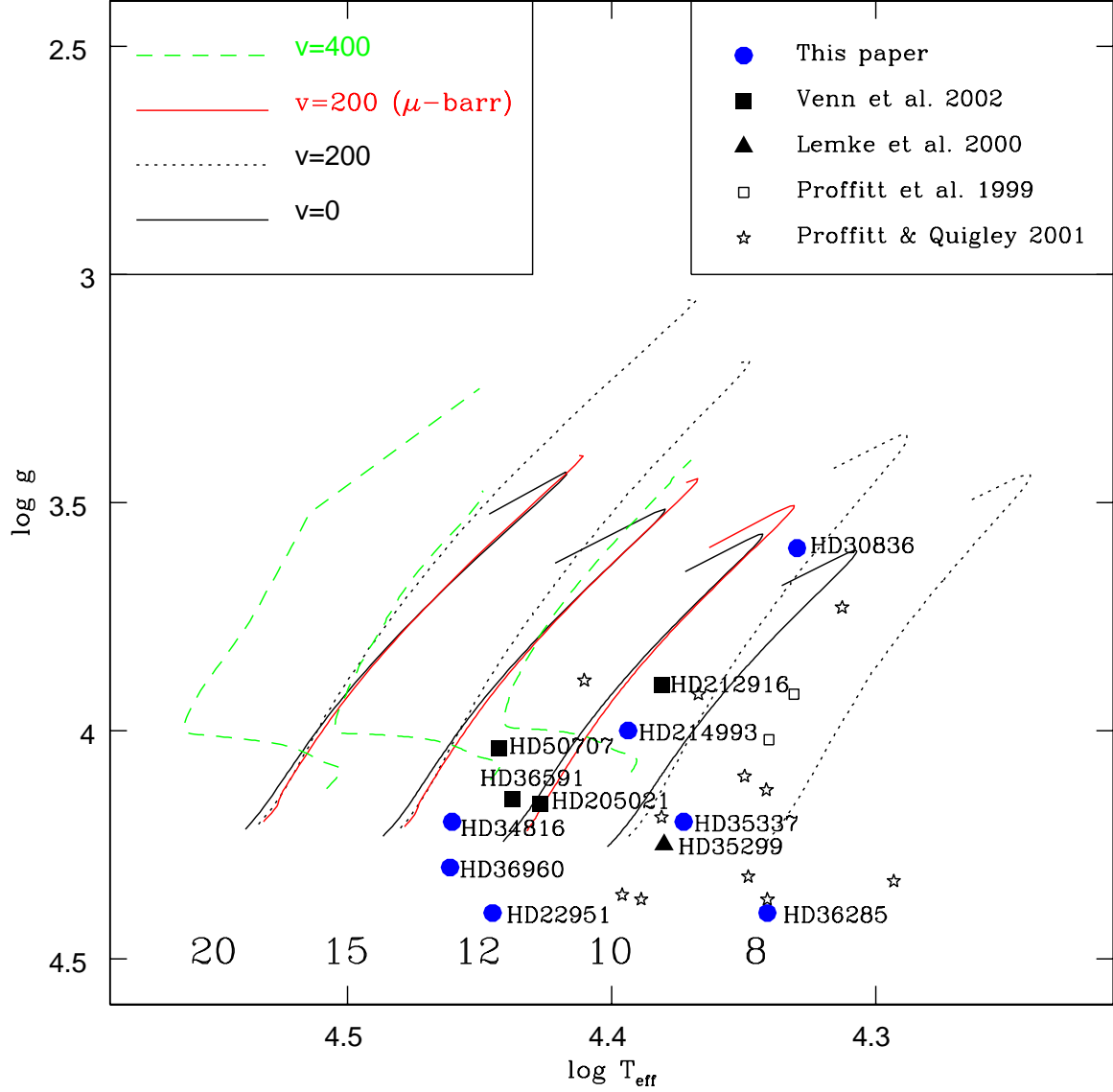
Fig. 7.— Temperature vs gravity to determine spectroscopic masses. Models with low (black line) to moderate rotation rates (dotted black line) and including μ-barriers (red line) are from Heger & Langer (2000). The effects of very rapid rotation on main-sequence position and thus spectroscopic mass can also be seen (green lines). Stellar masses associated with each model are labelled along the bottom of the figure. Only stars analysed in this paper and V02 are labelled. The temperatures of the stars have been scaled from their references to the Cunha & Lambert (1994) scale (see V02 for details).
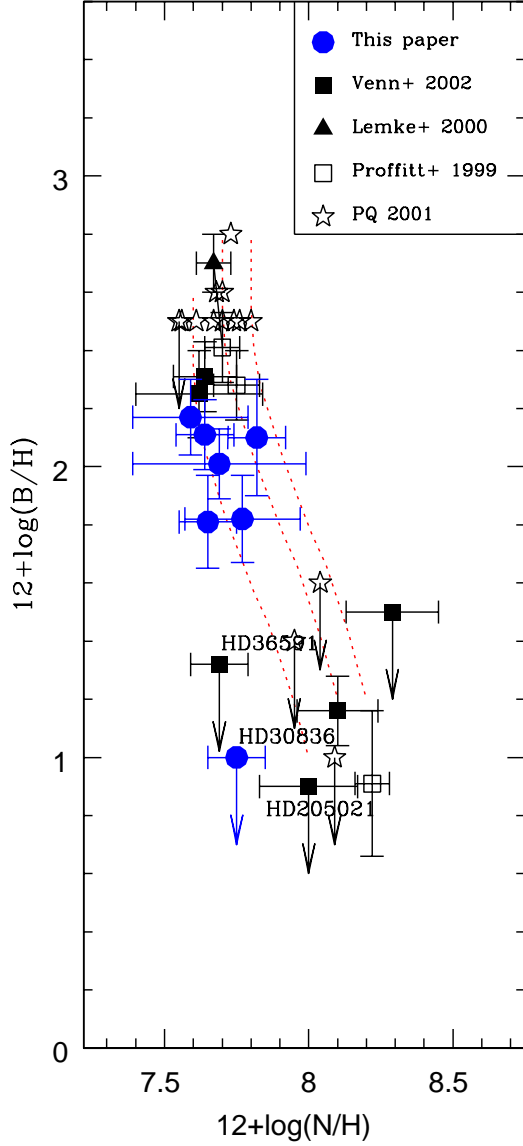
Fig. 8.— Boron and nitrogen abundances in B-stars. Note that these abundances have been corrected from their original references to a common temperature scale (see V02 for details). One rotating stellar evolution model is shown from Heger & Langer (2000); that for 12 $M_\odot$, V_{rot}=200 km s^{-1}, and including the μ-barrier (other masses and rotation rates have nearly identical predictions for the change in boron with nitrogen). The three dotted lines follow the predictions from this model for three different initial nitrogen and boron abundances; $(12+\log(N/H), 12+\log(B/H)) = (7.6, 2.6), (7.7, 2.7), (7.8, 2.8)$. The x-axis and y-axis are scaled equally to emphasize the destruction of boron before significant nitrogen enrichment.
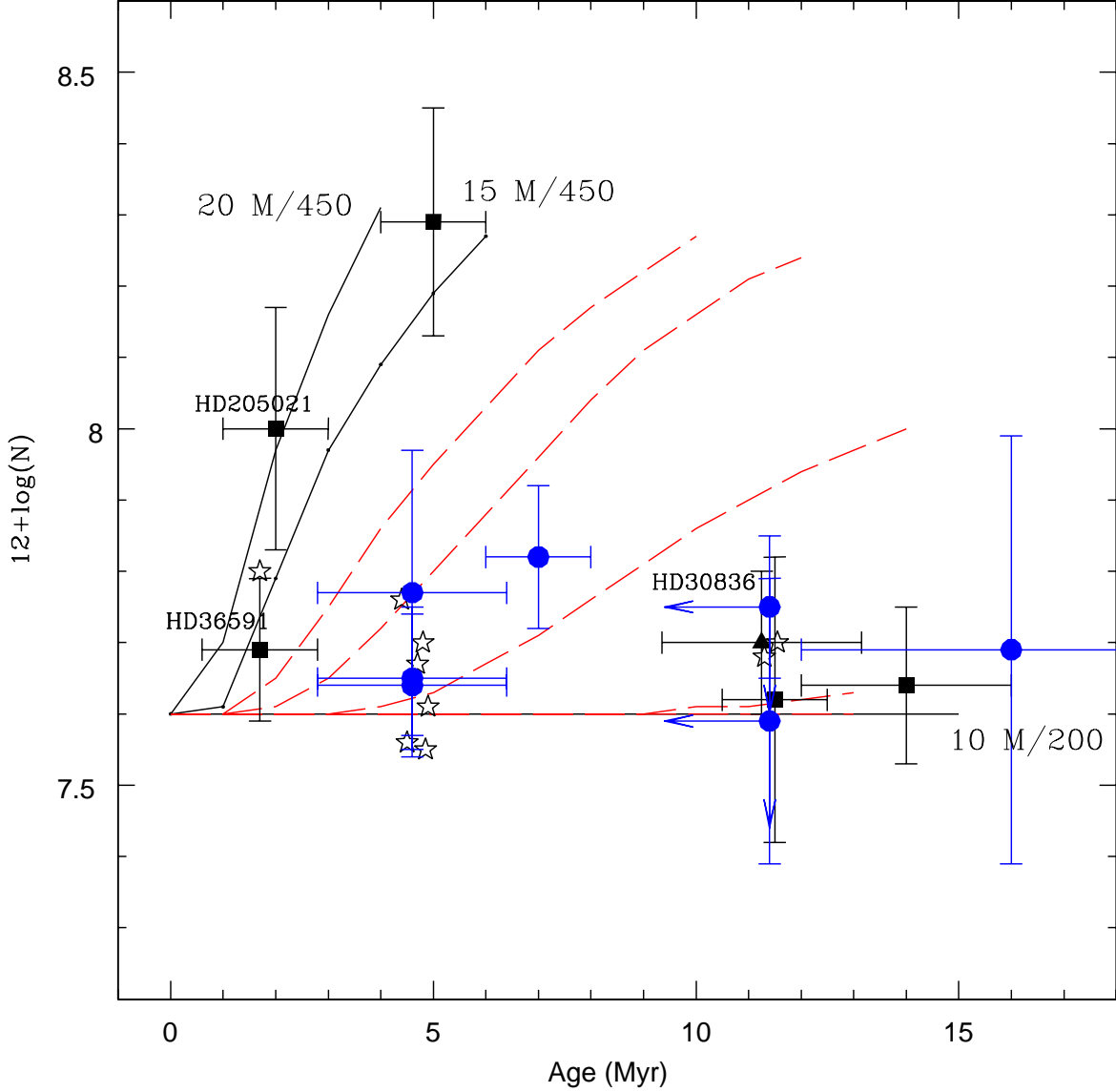
Fig. 9.— Nitrogen enrichment as a function of age. Data symbols the same as in Fig. 7. Rotating stellar evolution models are from Heger & Langer (2000). Red dashed lines represent $12 M_\odot$ models with various rotational velocities (0, 100, 200, 300, 450 km s^{-1}, where the lines for the slowest rotation rates lie along the bottom of the plot). Solid black lines represent 15 and $20 M_\odot$ models with the highest rotation rate (450 km s^{-1}), and a $10 M_\odot$ model with a moderate rotation rate (200 km s^{-1}).
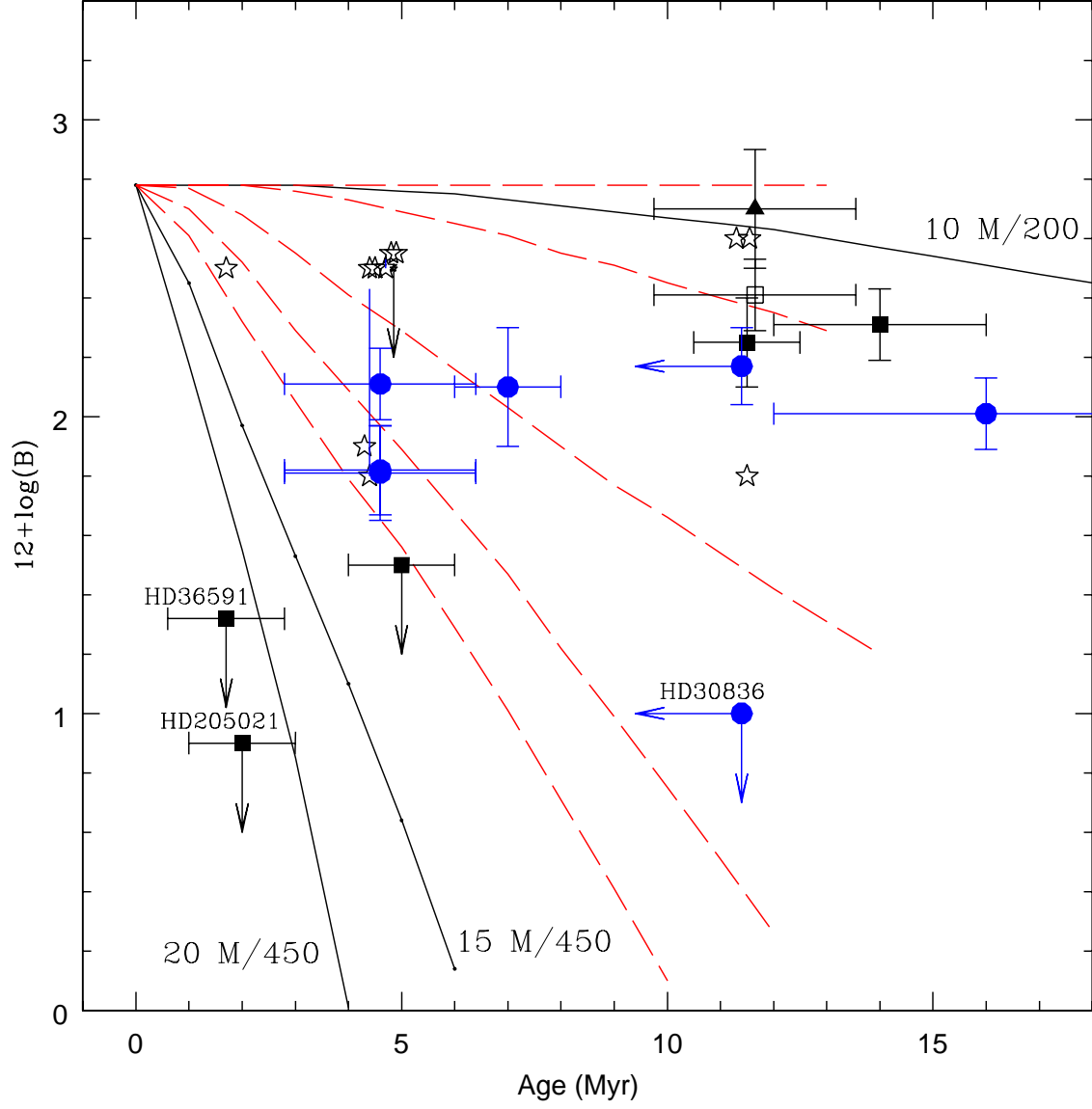
Fig. 10.— Boron depletion as a function of age. Data symbols the same as in Fig. 7. Rotating stellar evolution models are from Heger & Langer (2000). Red dashed lines represent $12M_\odot$ models with various rotational velocities (0, 100, 200, 300, 450 km s^{-1}). Solid black lines represent 15 and $20M_\odot$ models with the highest rotation rate (450 km s^{-1}), and a $10M_\odot$ model with a moderate rotation rate (200 km s^{-1}).